



Simulations of resonant modes in optical microcavities

THESIS

submitted in partial fulfillment of the
requirements for the degree of

BACHELOR OF SCIENCE

in

PHYSICS

Author :	D.G. Chobanova
Student ID :	s2895358
Supervisor :	Prof.dr. M.P. van Exter
Second corrector :	Dr. E.P.L. van Nieuwenburg

Leiden, The Netherlands, June 16, 2023

Simulations of resonant modes in optical microcavities

D.G. Chobanova

Huygens-Kamerlingh Onnes Laboratory, Leiden University
P.O. Box 9500, 2300 RA Leiden, The Netherlands

June 16, 2023

Abstract

Recent developments in the field of quantum optics have observed fine spectra in Fabry-Pérot microcavities that can be substantiated with theory. This thesis describes the development of a software that calculates the fine spectrum of a microcavity. A rotational-symmetric system is considered, with perfectly-reflecting mirrors. Paraxial theory states that these cavities have resonant modes in the form of scalar Laguerre-Gauss functions. Non-paraxial theory has added 2 scalar and 1 vector correction to the resonance frequencies. We use an object-oriented approach to propagate field profiles through a cavity with the help of Fourier transforms. Some numerical integration and interpolation tricks are used in the computations. Fine spectra are compared to theoretical predictions and a first step is made to finding the eigenfunctions of a cavity by modal decomposition. The software only provides scalar corrections and needs improvement in some areas, but shows promising results for the propagation correction. It could potentially lead to more advanced extensions, like a composite cavity which can help experimentalists to understand more complex resonance spectra.

Contents

1	Introduction	7
2	Theoretical framework	9
2.1	Preliminary concepts	9
2.1.1	Fabry-Pérot cavity geometry	9
2.1.2	Gaussian Beams	10
2.2	Field propagation	13
2.2.1	Slowly varying fields	13
2.2.2	Plane wave decomposition	13
2.2.3	Boundary conditions	14
2.3	Cavity resonances	15
2.3.1	Paraxial solutions	15
2.3.2	Non-paraxial corrections	16
2.4	Coupled modes	17
3	Simulation methods	19
3.1	General program remarks	19
3.2	Creating field profiles	20
3.2.1	Defining a cavity in Python	20
3.2.2	Normalized Laguerre-Gauss modes	20
3.3	Field propagation	22
3.3.1	Propagation options	22
3.3.2	Angular spectrum method	22
3.4	Modal decomposition	24
4	Results	25
4.1	Paraxial propagation	25
4.2	N=0 group	28
4.3	N=1 group	29
4.4	N=2 group	30
4.5	Modal decomposition	32

5	Discussion	35
5.1	Simulation challenges	37
5.2	Outlook	38
6	Conclusions	39
A	Alternative route: Finite element analysis	41
B	Supplementary documentation on the simulation program	43
B.1	Objects file	43
B.1.1	Geometry	43
B.1.2	Field	43
B.1.3	Mode	44
B.1.4	Other routines outside classes	45
B.2	Plot routines file	45
B.2.1	plot_intensity	45
B.2.2	plot_mirr	45
B.2.3	plot_plane	45
B.2.4	plot_decomposition	45
B.3	Main file	46

Introduction

Optical microcavities are widely used tools in optics, for example as a spectrum analyzer [1] or to trap light between two highly-reflecting mirrors [2]. These microcavities are Fabry-Pérot (FP) cavities that are only a few wavelengths long, and have at least one mirror with a radius of curvature $R_m < 100\lambda$. A paraxial description predicts that the resonance spectrum of such a cavity consists of equidistant peaks [3]. It also predicts that groups with the same longitudinal mode number q and transverse order N - so-called (q,N) groups - are frequency degenerate. However, recent developments in the field have made new observations [4]: (q,N) groups show slightly different resonance frequencies for different radial numbers p , orbital angular momentum (OAM) numbers l , and polarizations ν . This splitting in resonance frequencies is a so-called a fine spectrum and arises from nonparaxial effects. These nonparaxial effects can be seen as a perturbation in the Hamiltonian, just like atoms show a fine spectrum when taking, for example, relativistic corrections into account. It is intriguing to note that cavity resonances show the same nature as atoms.

The nonparaxial description of electromagnetic waves has been studied since the seventies and is still a problem being discussed today. Lax [5] was the first to rewrite the Maxwell equations into a form that takes into account nonparaxial effects. When reformulating the problem, it is equally important to reformulate the boundary conditions for these nonparaxial effects as well. These conditions require the wavefront at the mirror surface to have the same curvature as the mirror. This is also called the resonance condition. In the eighties, a basis for nonparaxial theory was developed. Erickson [6], calculated a scalar nonparaxial correction to the resonances. Later, Cullen [7] and Davis [8] added a vector correction. Yet still, a full picture was missing. Yu and Luk [9] combined these corrections into a complete analysis of FP resonance spectra. Van Exter [10] has most recently provided

a general theoretical framework that uses perturbation theory to find non-paraxial effects that induce a fine spectrum in the cavity resonances, which has been supported by experimental observations [4].

This thesis provides a numerical description of the problem. A rotational-symmetric, perfectly-reflecting cavity is considered such that effects due to mirror roughness, such as the Bragg effect can be neglected. Using the rotational symmetry, the problem could be reduced to 2 dimensions. The problem is solved using the angular spectrum method [11], where an attempt is made to quantify the nonparaxial effects at a curved mirror. A Python software is presented that calculates the scalar nonparaxial effects by switching different propagation options on and off. Also, a first step is made in calculating the eigenmodes of the cavity.

In chapter 2, a theoretical framework is provided for the cavity, describing key equations for the problem with according boundary conditions as well as theoretical predictions for the fine spectrum. Chapter 3 describes the various simulation methods, followed by the obtained results in chapter 4. Challenges, lessons learned and the outlook are discussed in chapter 5, finalizing with a summary and conclusion in chapter 6. Two appendices are included, appendix A derives an alternative route for solving the propagation problem and appendix B provides supplementary code documentation to chapter 3.

Theoretical framework

2.1 Preliminary concepts

2.1.1 Fabry-Pérot cavity geometry

Consider a perfectly-reflecting, rotational-symmetric, plano-concave Fabry-Pérot microcavity, presented in Figure 2.1. Such a cavity has a plane mirror placed at $z=0$, and a concave mirror with radius of curvature R_m at $z=L$, L being the cavity length. The z coordinates of the mirror $z = L - z_m$ are found by Equation (2.1)

$$z_m(r) = R_m - \sqrt{R_m^2 - r^2} \quad (2.1)$$

We distinguish spherical and aspherical mirrors, by taking a Taylor expansion around $r=0$

$$z_m(r) = \frac{r^2}{2R_m} + \frac{r^4}{8R_m^3}(1 - \tilde{p}) \quad (2.2)$$

where a geometric parameter \tilde{p} is introduced to represent the shape of the mirror. For a spherical mirror $\tilde{p} = 0$ and for a parabolic mirror $\tilde{p} = 1$. [10]

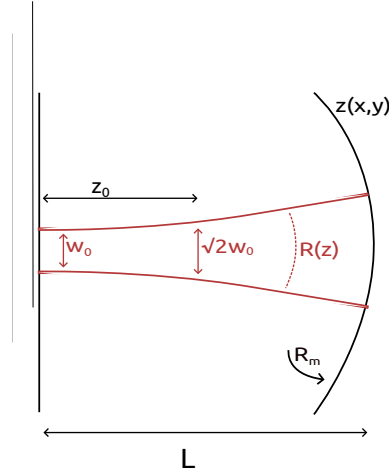


Figure 2.1: Plano-concave Fabry P rot microcavity. A plane mirror is placed at $z=0$ and a concave mirror with radius of curvature R_m and $z=L$, the cavity length. A Gaussian beam with initial width w_0 and Rayleigh range z_0 propagates through the cavity. The radius of curvature of the Gaussian beam throughout the cavity is given by $R(z)$

Such a cavity provides a series of sharp resonance peaks, visible as a transmission spectrum, for specific combinations of cavity length L and wavelength λ . The resonant modes are Gaussian modes, this is derived in section 2.3. The next section describes these modes in more detail.

2.1.2 Gaussian Beams

We use the complex source method [1] to describe Gaussian beams. They propagate through space as

$$E(r, z) \propto \frac{1}{q(z)} \exp\left(\frac{ikr^2}{2q(z)}\right) \exp(ikz) \quad (2.3)$$

where

$$\frac{1}{q(z)} = \frac{i}{\sqrt{z^2 + z_0^2}} \exp\left[-i \arctan(z/z_0)\right] \frac{1}{R(z)} + i \frac{\lambda}{\pi w(z)^2} \quad (2.4)$$

is the Gaussian beam parameter, which is related to the other characteristics of Gaussian beams [12]:

1. Beam waist w_0
2. Beam width $w(z) = w_0 \sqrt{1 + \left(\frac{z}{z_0}\right)^2}$

3. Rayleigh range $z_0 = \frac{1}{2}kw_0^2 = \frac{\pi}{\lambda}w_0^2$

4. Radius of curvature $R(z) = z \left[1 + \left(\frac{z_0}{z} \right)^2 \right]$

5. Gouy phase $\chi = \arctan(z/z_0)$

A Gaussian beam starts with a beam waist w_0 , which increases upon propagation, depending on the Rayleigh range. The Rayleigh range represents the distance where $w(z)$ has become $\sqrt{2}$ times bigger than w_0 . As the wave propagates, the wavefront becomes curved, with a radius $R(z)$ given above. As the beam propagates, it also acquires a phase lag, which is represented by the Gouy phase. The beam propagation is also represented in Figure 2.1. It is useful to rewrite some beam parameters as functions of the cavity length L and the concave mirror's radius of curvature R_m . We now have $z_0 = \sqrt{L(R_m - L)}$, $w_0 = \sqrt{(\lambda z_0 / \pi)}$.

Equation (2.3) represents the fundamental Gaussian mode, which is a 2D Gaussian function in the x and y direction. Higher order modes also occur, in the form of Hermite-Gaussian (HG) and Laguerre-Gaussian (LG) modes. In the simulations, rotational symmetry will be used which makes LG modes a convenient basis. LG modes are generalized Laguerre polynomials $\mathcal{L}_p^\ell(x)$, that satisfy the following differential equation

$$xy'' + (\ell + 1 - x)y' + py = 0 \quad (2.5)$$

with $x = r^2$ in cylindrical coordinates. Figure 2.2 shows the intensity profiles of some LG modes for different quantum numbers ℓ and p . The 00 mode is the fundamental mode, described by Equation (2.3).

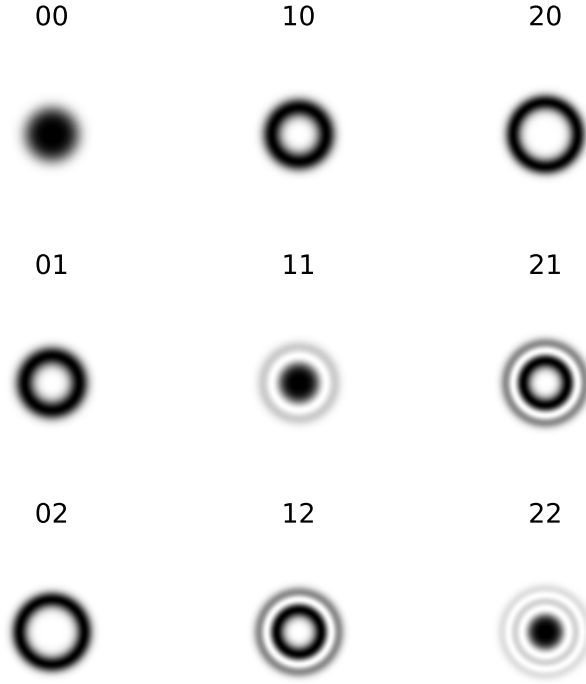


Figure 2.2: Intensity profile of Laguerre-Gaussian($LG_{p\ell}$) modes. The LG modes are characterized by the number of nodes in the radial direction p and the azimuthal quantum number ℓ . The fundamental (00) mode is the upper left. Figures generated in Python.

Laguerre polynomials are orthogonal over e^{-x} , which makes LG modes an orthogonal basis. For this research purpose, the modes will also be normalized, meaning they have power 1. The modes are normalized by

$$\langle \psi_{p,\ell}^+ | \psi_{p,\ell}^+ \rangle = \int_0^{2\pi} d\theta \int_0^r dr |\psi_{p,\ell}^+(r, \theta, z)|^2 = 1 \quad (2.6)$$

The normalization constant is

$$|A|_{p\ell}^{LG} = (-1)^p \left(\frac{p!}{\pi(l+p)!} \right)^{1/2} \quad (2.7)$$

Here, $p = \min(n, m)$ and $\ell = n - m$ [13]. Making the modes have power 1, gives an easy check for the propagation, which must be power conservative, or in other words a unitary operation.

2.2 Field propagation

2.2.1 Slowly varying fields

When dealing with wave optics, the goal is to solve the Helmholtz equation with some boundary conditions.

$$(\Delta + \vec{k}^2) \vec{E} = 0 \quad (2.8)$$

with $\Delta = \frac{\partial^2}{\partial x^2} + \frac{\partial^2}{\partial y^2} + \frac{\partial^2}{\partial z^2}$ the Laplace operator, \vec{k} the wave vector and \vec{E} the electric field. We define the optical axis or propagation direction in the $\pm z$ direction. In the paraxial approximation, this can be rewritten as the following product [5], where we only take the forward-propagating wave into account. The backward-propagating wave is just its complex conjugate.

$$\vec{E} = \vec{\psi}^+(\vec{r}, z) \cdot e^{ikz} \quad (2.9)$$

Equation (2.8) can be rewritten as

$$\Delta_{\perp} \vec{\psi}(\vec{r}) + 2ik \frac{\partial}{\partial z} \vec{\psi}(\vec{r}) + \frac{\partial^2}{\partial z^2} \vec{\psi}(\vec{r}) = 0 \quad (2.10)$$

where

$$\Delta_{\perp} = \frac{\partial^2}{\partial x^2} + \frac{\partial^2}{\partial y^2} = \frac{\partial^2}{\partial r^2} + \frac{1}{r} \frac{\partial}{\partial r} + \frac{1}{r^2} \frac{\partial^2}{\partial \theta^2} \quad (2.11)$$

This is the slowly-varying Helmholtz equation.

$$\psi(\vec{r}) = \psi_{\perp}(\vec{r}) + \psi_z(\vec{r}) \cdot \vec{e}_z \quad (2.12)$$

Maxwell's divergence equation $\vec{\nabla} \cdot \vec{E} = 0$ becomes

$$ik\psi_z + \vec{\nabla}_{\perp} \cdot \psi_{\perp} + \frac{\partial}{\partial z} \psi_z = 0 \quad (2.13)$$

Equations (2.9) and (2.13) are exact and contain no approximations. A description of the propagation of the transverse and longitudinal electric fields has been provided, and hence the full problem is described. At the flat mirror, the boundary condition demands $\vec{E}_{\perp} = 0$, which corresponds to $\psi_{\perp}(\vec{r})$ is purely imaginary at $z=0$. The paraxial form of Equation (2.10) is

$$\Delta_{\perp} \vec{\psi}(\vec{r}) + 2ik \frac{\partial}{\partial z} \vec{\psi}(\vec{r}) = 0 \quad (2.14)$$

2.2.2 Plane wave decomposition

An alternative way to describe the propagation of an optical field is through the plane-wave decomposition of the electric field at $z=0$ [14].

$$\vec{E}_k(k_x, k_y) = \iint \vec{E}(x, y, z=0) e^{-i(k_x x + k_y y)} dx dy \quad (2.15)$$

This is the 2D Fourier transform of the electric field, which will further be denoted as $\text{FFT2D}\{\vec{E}\}$. The field at arbitrary z is then found by the inverse Fourier transform of the electric field in k -space, multiplied by the wave vector $e^{ik_z \cdot z}$. The z -component of the k -vector is

$$k_z = \sqrt{k^2 - k_{\perp}^2} \approx k - \frac{k_{\perp}^2}{2k} - \frac{k_{\perp}^4}{8k^3} + \text{higher order terms} \quad (2.16)$$

The first order term shows the paraxial contribution to the propagation, and all higher order terms are non-paraxial contributions, which are further described in section 2.3.2 The electric field is then given by

$$E(x, y, z) = \frac{1}{(2\pi)^2} \iint \vec{E}_k(k_x, k_y) \cdot e^{ik_z \cdot z} \cdot e^{-i(k_x x + k_y y)} dk_x dk_y \quad (2.17)$$

Writing this in terms of Fourier transforms, the electric field at z is

$$E(x, y, z) = \text{IFFT2D} \left\{ \text{FFT2D} \{E(x, y, 0)\} \times e^{ik_z \cdot z} \right\} \quad (2.18)$$

2.2.3 Boundary conditions

In a perfectly reflecting cavity, a resonant mode is found by looking for a mode that stays the same after completing a round trip, which is called the resonance condition. This indicates how much we should change the frequency of the light to make it 'fit' in the cavity. We require the definition of some boundary conditions to find the resonance condition. A distinction is made between scalar and vector boundary conditions.

The scalar boundary condition demands that at the mirror, $E_{\perp}(r, z) = \text{Re}[\psi(r, z)] = 0$. Another way to formulate this, is that the shape of the wavefront $z_{\text{wave}}(r)$ should match the shape of the mirror $L - z_m$ and that the phase should be an integer multiple of $\pi/2$. The shape mismatch is defined as $\Delta z = z_m - z_{\text{wave}}$ [10]. However, the cavity typically does not contain an integer number q of half wavelengths or in other words, the phase on the mirror surface is not $\pi/2$ modulo π . To fix this issue, a uniform phase mismatch can be used as a measure of resonance frequency.

The vector boundary condition is $\vec{E}_{\parallel} = 0$ at the mirror, where \vec{E}_{\parallel} is the component of the electric field parallel to the mirror. This results in a scalar azimuthal boundary condition $E_{\theta} = 0$, and a radial boundary condition

$$E_{\parallel, r} = E_r - \frac{r}{R_m} E_z = 0 \quad (2.19)$$

This condition shows that there is an extra, transverse projected, field being created at the mirror that is oriented in the radial direction. It predicts, for example, that for spherical mirrors the resonant mode requires a slightly elliptical beam with beam waists $w_x \neq w_y$.

2.3 Cavity resonances

2.3.1 Paraxial solutions

As the full problem has been described, we can look at expected solutions to the equations. Equations (2.10) and (2.13) can be simplified, by neglecting all higher order terms of $\frac{\partial}{\partial z}$. This is called paraxial propagation, and now the propagation equations have been reduced to

$$\Delta_{\perp} \psi(\vec{r}) \approx -2ik \frac{\partial}{\partial z} \psi(\vec{r}) \quad (2.20)$$

$$\psi_z \approx \frac{i}{k} \vec{\nabla}_{\perp} \cdot \psi_{\perp} \quad (2.21)$$

Equation (2.20) resembles the Schrödinger equation, where z acts as a time coordinate. The factor i shows that a slowly-varying field acquires a phase lag when propagating. On-axis (at $r=0$), this appears as a Gouy phase lag, and off-axis this is the wavefront curvature [10].

In a rotational symmetric cavity, this equation has an exact solution of the form

$$\Psi(r, \theta, \chi) = f(p, \ell) e^{i\ell\theta(N+1)\chi} \quad (2.22)$$

with $f(p, \ell)$ the normalized radial amplitude function

$$f(p, \ell) = |A|_{lp}^{LG} r^{\ell} L_p^{\ell}(r^2) \exp(-r^2/2) \quad (2.23)$$

$|A|_{lp}^{LG}$ is described by Equation (2.7). So the paraxial equation has a basis of LG modes as a solution. These solutions are exact and can be computed analytically [10], hence we have a prediction for what the modes should look like at the curved mirror.

The expected phase on-axis, at the mirror ($z=L$) is given by the Gouy phase, at $z=L$. Using the Gaussian beam characteristics, we can predict a single-pass phase

$$\phi_{parax} = \arctan\left(\frac{L}{z_0}\right) = \arctan(\sqrt{L/R_m - L}) \quad (2.24)$$

where ϕ_{parax} is the Gouy phase, also denoted as the paraxial phase.

2.3.2 Non-paraxial corrections

References [4] and [10] describe three different non-paraxial effects, which together form the fine structure of the cavity: propagation correction, wave-front correction, and vector correction. These corrections are quantified as a phase delay

$$\varphi = kL - \phi(r, z) \quad (2.25)$$

which is the difference between the phase of a plane wave at $z=L$ and the forward-propagating, slowly-varying field.

The propagation correction originates from the Taylor expansion of k_z in Equation (2.16). Filling this into the propagation equation (2.17) for $r=0$ and $z=L$ (on-axis), we get

$$E(r=0, z=L) = \iint E(k_x, k_y) \exp(ik_z L) dk_x dk_y \quad (2.26)$$

This results in a single-pass phase lag of

$$\begin{aligned} \Delta\phi &= \phi_{parax} - \phi_{prop} = -\langle \frac{k_{\perp}^4}{8k^3} \rangle L \\ &= -\frac{f(p, \ell)}{8kR_m} \frac{R_m}{R_m - L} \end{aligned} \quad (2.27)$$

which suggests a slight increase in the Gouy phase, by a polynomial $f(p, \ell)$ [9, 10]. The brackets denote a projection on profiles, which is equivalent to averaging over the modal intensity.

$$\langle x \rangle = \langle \psi_i | x | \psi_i \rangle = \iint x |\psi_i|^2 dx dy \quad (2.28)$$

It is then important to note that the phase lag acts upon the average phase of the field profile

$$\phi_{avg} = \langle \phi \rangle \quad (2.29)$$

We can also define the root mean square (RMS) phase, which shows how much the phase deviates from the average. This will be used as an error estimate

$$\phi_{RMS} = \sqrt{\langle \phi^2 \rangle} \quad (2.30)$$

The phase lag is also dependant on the mode numbers p and ℓ , given by $f(p, \ell)$ in (2.31) below

$$f(p, \ell) = \frac{3}{2}(N+1)^2 - \frac{1}{2}(\ell^2 - 1) \quad (2.31)$$

The number $\frac{1}{8k(R_m-L)}$ is an important expansion parameter and will further be denoted as the relative strength of the non-paraxial effects.

The wavefront correction follows from a different Taylor expansion: that of $\chi(z)$ and $R(z)$ around a paraboloidal reference surface $z = L - r^2/2R_m$, such that [10]

$$z_{wave} = \frac{r^2}{2R_m} + \frac{2(N+1)}{k^2 w_0^2} \frac{r^2}{2R_m} - \frac{r^4}{4R_m^2 L} \left(1 - \frac{2L}{R_m}\right) \quad (2.32)$$

The first term corresponds to the paraxial wavefront curvature. The second and third terms show corrections with respect to the paraxial curvature. The second term shows that the r^2 component of the wavefront is slightly larger than the paraxial wavefront. The third term quantifies an r^4 component of the wavefront, which shows that the outer regions of the paraxial wavefronts are "flatter than paraboloidal". Reference [10] also considers deviations from a spherical mirror, to the more general mirror shape

$$z_m \approx \frac{r^2}{2R_m} + \frac{r^4}{8R_m^3} (1 - \tilde{p}) \quad (2.33)$$

Based on the previously introduced parameter \tilde{p} in section 2.1.2. The wavefront correction can be written as a single-pass phase lag

$$\Delta\varphi = \langle k\Delta z_{wave} \rangle = -\frac{f(p, \ell)}{8kR_m} \frac{\tilde{p}L}{R_m - L} \quad (2.34)$$

The vector correction originates from the extra projected longitudinal field described in section 2.2.3. The longitudinal field is out of phase with the transverse field, which induces a frequency shift. The shift calculated in reference [10] and is equal to

$$\Delta\varphi = \frac{-1 - \ell \cdot s}{8kR_m} \quad (2.35)$$

where s is the spin angular momentum, equal to ± 1 .

The combined effects of the three corrections yield a roundtrip phase lag

$$\varphi_{fine} = \frac{1}{kR_m} \left[\frac{1}{8}(N^2 + 2N - 4) - \frac{3}{8}\ell^2 - \ell \cdot s \right] \quad (2.36)$$

A smaller phase lag, means that there is less phase delay and a larger phase at the mirror. This requires a shorter cavity length or lower frequency to reach resonance.

2.4 Coupled modes

The phase shifts described in the previous section are for the $\Delta p = 0$ modes, but non-paraxial propagation also results in mode coupling to modes with

$\Delta p = \pm 1$ and $\Delta p = \pm 2$ [6]. The strength of this coupling is proportional to $f(p, \ell)$ defined in Equation (2.31). The couplings are associated with perturbations $\propto r^4$ and $k_\perp^4 = -\Delta_\perp^2$. By applying this operator twice, the couplings can be calculated [10].

$$\begin{aligned}
\langle \Psi_{p-1, \ell} | \Delta_\perp^2 | \Psi_{p, \ell} \rangle &= -4p \sqrt{p(p + \ell)} \\
\langle \Psi_{p+1, \ell} | \Delta_\perp^2 | \Psi_{p, \ell} \rangle &= -4(p + 1) \sqrt{(p + 1)(p + \ell + 1)} \\
\langle \Psi_{p-2, \ell} | \Delta_\perp^2 | \Psi_{p, \ell} \rangle &= \sqrt{p(p - 1)} \sqrt{(p + \ell)(p + \ell - 1)} \\
\langle \Psi_{p+2, \ell} | \Delta_\perp^2 | \Psi_{p, \ell} \rangle &= \sqrt{(p + 1)(p + 2)} \sqrt{(p + \ell + 1)(p + \ell + 2)}
\end{aligned} \tag{2.37}$$

We now know that the dominant ($\Delta p = 0$) mode acquires a single-pass phase shift with a strength shown in Equation (2.36). Other modes with $\Delta p = \pm 1$ and ± 2 mix in with amplitudes given by dimensionless factors in Equation (2.37) multiplied by $1/8k(R_m - L)$. This is a first step in finding the ‘real’ eigenmodes of the cavity, which can be written as a linear combination of paraxial modes

$$\Psi(r, \theta) = \sum_j \alpha_j \Psi_j \tag{2.38}$$

where α_j are the coupled mode amplitudes. We expect that for the dominant mode, this amplitude is ≈ 1 and a small mixing of other modes. A constraint for α is

$$\sum_j |\alpha_j|^2 = 1 \tag{2.39}$$

Chapter 3

Simulation methods

This chapter discusses the key simulation methods used for the computation of the fine spectrum. The full code and documentation can be found on Github and in Appendix B

3.1 General program remarks

Initially, an attempt was made to solve the modified Helmholtz equation (2.10) using numerical methods for differential equations [15]. In Appendix A, the discretization of the equation is derived. We quickly found out that such a discretization causes a lot of difficulties. The off-diagonal elements of the propagation matrix for one step Δz are really small in comparison to the diagonal elements. This makes the propagation matrix almost equal to the identity matrix. With each step, this matrix is multiplied by itself again, making these effects stronger. In the end, what we thought we had defined as propagation, gave the exact same mode after propagating to the mirror. We decided to move on to the plane wave decomposition, which provided more potential for finding the fine structure.

Propagation with the plane wave decomposition provided a lot of errors that had to be traced back somewhere in the code. The 'main' program was messy due to the many changes we had implemented and hard to navigate through. A choice was made for an object-oriented programming approach. The program was rewritten completely from scratch. The object-oriented code made the process of localizing and fixing errors much easier and the main program could now be run in just a couple of lines. Plot routines were also put in a separate file to make the code more readable.

The object-oriented program consists of a number of important classes:

Geometry, Field, that has a 1D and 2D variant, and Mode. The Geometry class is a base class for all other objects which inherit the geometric parameters of the cavity. The splitting between Field1D and Field2D objects made the process of figuring out the dimension of the field profile used much easier. The last object, Mode, contains the most important parameters and methods. It defines the initial mode profile at the flat mirror ($z=0$) and contains the propagation methods.

3.2 Creating field profiles

3.2.1 Defining a cavity in Python

Before the propagation of a field profile was implemented, some geometric parameters needed to be defined. To achieve this, a class Geometry was made, which contains all important parameters that define the problem. These are the wavelength λ , wave vector \vec{k} , cavity length L , radius of curvature R_m and mirror shape parameter \tilde{p} . From these parameters, the Rayleigh range z_0 and initial beam width w_0 could be calculated, as defined in section 2.1.1. Another important parameter defined in the class is the grid size. This determines how many points are in the array of x and y coordinates on which the field is created. The x and y grids were chosen to be identical, as rotational symmetry is used. They range from $-x_{\max}$ to x_{\max} on an odd grid, such that the origin is also present in the array. The choice of x_{\max} is dependent on w_0 , which is further explained in section 3.2.2.

3.2.2 Normalized Laguerre-Gauss modes

Another class Mode was created, which takes mode numbers p, ℓ and N as arguments as well as a Geometry object and a boolean variable 'paraxial', that determines whether or not the mode propagates paraxially or non-paraxially. This class has a method `field_profile` that with the help of Numpy's `eval_genlaguerre` method [16] and Equation (2.7) calculates the normalized field profile at $z=0$. This is returned as Field object that contains a 2-dimensional array with the field profile values at each x and y coordinate.

To check if the fields are normalized well, the power was calculated. The power of the field is given by Equation (2.6). As the cavity is rotationally symmetric, the integral over θ gives 2π . To calculate the integral over r , a 1D cross-section of the field at $y=0$ was taken ($x=0$ would yield the same answer, but a choice was made for $y=0$). Here, the field has its highest intensity and the power should be 1. There are lots of possibilities

to compute an integral numerically: finite sum, trapezoidal rule, Romberg rule, mid-point rule, ... It is also possible to implement a Cubic Spline interpolation to compute an integral [15]. This method gave the best results and was used for all numerical integrals that had to be computed. Previously was noted that an appropriate grid size is needed. Numerical errors of order $(N - 1)^{-n}$ occur when computing an integral, where N is the grid size and n is some positive exponent. This was tested for the cubic spline method.

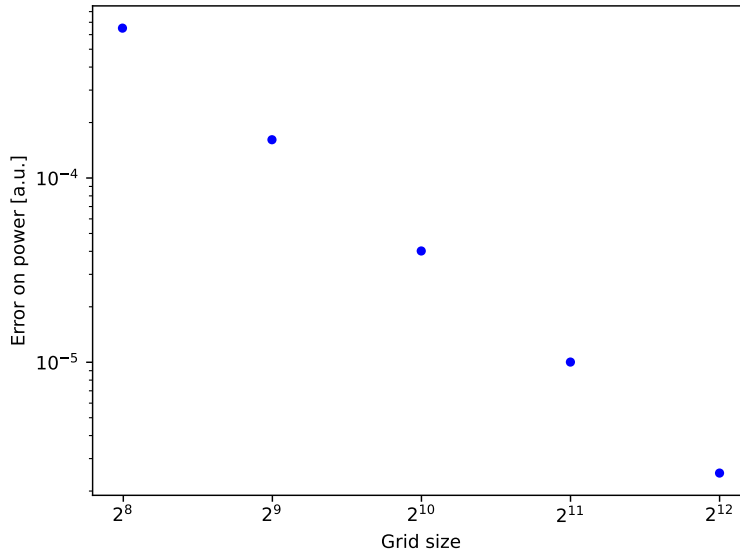


Figure 3.1: Error on power calculation of the normalized $N=0$ mode as a function of the grid size.

On a logarithmic scale, we see a linear decrease in error, which was defined as 1-power, as the expected power is 1. A quick fit to the line shows a slope of -2, which indicates a quadratic decrease in error as the grid size doubles. However, a higher grid size has a cost: computation time. Table 3.1 below shows the computation time of one propagation to the mirror (the propagation method and calculation are explained later in section 3.3.2) for several grid sizes.

Table 3.1: Computation time for one propagation to the mirror surface

Grid size	Computation time [s]
255	0.030
511	0.14
1023	0.60
2047	4.78
4095	11.50

Although a grid size of 4095 introduces an error of order 10^{-6} , as opposed to 10^{-5} for 2047, a choice was made for the smaller grid, because the time cost for increasing the grid size is too large.

3.3 Field propagation

3.3.1 Propagation options

The program provides two of switches, so we can test several scenarios: paraxial ON/OFF and mirror ON/OFF. Firstly, paraxial propagation (paraxial ON) to a plane mirror (mirror OFF) should give an exact result, as this problem can be solved analytically (see section 2.3.1). After propagation, the phase of the field is corrected for the mirror curvature, so $k \cdot z_m(r)$ is subtracted [17]. Nonparaxial propagation (paraxial OFF) to a plane mirror (mirror OFF), also after phase correction, should yield the propagation correction given by Equation (2.27). Lastly, nonparaxial propagation (paraxial OFF) to a curved mirror (mirror ON) should yield the sum of the propagation and wavefront correction (2.34). A third switch can be added: vector ON/OFF. This will include the vector effects and complete the fine structure of the cavity. Such a switch is not included yet, so the vector corrections are still missing.

3.3.2 Angular spectrum method

Based on the plane wave decomposition and 2.18, a method was developed to propagate the field from $z=0$ to the mirror. Firstly, we discuss how the Fourier transform (FFT) was implemented. Then, plane mirror propagation is described in more detail, followed by curved mirror propagation.

Scipy's `fftpack` module [18] was used to compute the FFTs in a method called `FFT2D`. An important part of the computation was to find k_z . The `fftfreq` method returns the Fourier frequencies without the factor 2π . These frequencies were called \bar{k}_x and \bar{k}_y . Their spacing in Fourier space is $\frac{\text{grid size}}{2x_{\max}}$.

As the grid size is already determined based on power calculation, the parameter x_{\max} plays an important role in how many points in Fourier space are relevant for the calculation. As the field profile decreases with r^2 , a very large x_{\max} means that a lot of the points on the grid are wasting memory due to the field being 0 and not giving more accurate results. If x_{\max} is too small, not enough points in Fourier space can account for the field and the FFT will become unstable. The x range should be at least a couple of times the beam waist w_0 so that the beam 'fits' inside the grid. For higher order N modes, it takes a longer time for the field to decrease to 0, so the scaling of x_{\max} was chosen $\propto w_0\sqrt{N+1}$. The ideal value was found to be $5w_0\sqrt{N+1}$. Now that x_{\max} has been determined, the frequencies can be calculated. The propagation method also takes a parameter 'paraxial' as an argument, which determines whether the propagation should be paraxial or nonparaxial. If paraxial, k_z is taken to be the Taylor expansion of Equation (2.16), with terms up to k_{\perp}^4 . If nonparaxial, the full square root is taken to find k_z . With k_z , the propagation vector can be computed: $\exp(ik_z)$. Now, (2.18) can be applied using fftpack's `fft2` and `ifft2` methods.

The propagation to the plane mirror is computed by a single Fourier transform to the $z=L$ plane. It is known that the beam has a curvature and is not a plane wave. This is accounted for by a factor $\exp[ikz_m(r)]$, where $z_m(r)$ is given in Equation (2.1). Propagation routines return a `Field` object with a one-dimensional array of field profile elements. The cross-section at $y=0$ is taken, just as in the power calculations. This is possible because the fields are rotational-symmetric and are the same in the x- and y-direction.

The propagation to the curved mirror is a bit more complicated. As the mirror coordinates are dependent on r , direct computation with the plane-wave decomposition is not possible. The curvature of the mirror has to be accounted for. This is done by using an interpolation technique. An integer number $n > 1$ z-planes are taken 'close' to the mirror. Close is determined by x_{\max} . A variable z_{\min} is introduced

$$z_{\min} = L - R_m + \sqrt{R_m^2 - x_{\max}^2} \quad (3.1)$$

Then, an array of z-planes is made to which the field is propagated. These are n evenly spaced planes going from z_{\min} to L . As in the plane mirror propagation, with each plane the $y=0$ cross-section is taken and the field is returned as a `Field` object. After this, a cubic spline interpolation [15, 18] is carried out. This gives an array of length grid size that contains the field profiles at the z-coordinates of the mirror. Note that when n is taken to be equal to the grid size, the interpolation will be useless. Out of this array of field profiles, the diagonal elements correspond to the field at the mirror's surface. The choice of n is quite ambiguous. If it is very large, the interpo-

lation will yield a more accurate result, as it has more points to work with. But a large number of Fourier transforms is very time-consuming. A single propagation computes 2 2D Fourier transforms on an $N \times N$ grid. A single 2D fft costs $N^2 \log_2 N^2$ computations [19]. For a grid size of 2047, this is almost 10^8 . If this has to be done $2N$ times, this means that the number of computations is of order N^3 . This costs a lot of computational power. After some tests, a value of $n=4$ was found to give the same results as a value of $n=N$, decreasing the number of computations drastically. Interpolation is luckily a fast computation and does not cost a lot of time. It just creates a continuous function based on known values and fills in the rest using a third-order polynomial. This field is also corrected for the mirror curvature and thus multiplied by a factor $\exp[ikz_m(r)]$. The resonance condition stated in the theory section, says that a uniform phase mismatch is wanted at the mirror. Another way to put this, is that after subtraction of the average phase, the phase of the field should be 0 for all r . Note that the phase is defined to be $\in [-\frac{\pi}{2}, \frac{\pi}{2}]$.

3.4 Modal decomposition

Equation (2.37) represents the predicted mode couplings at the mirror surface. This can be computed using numerical integration, using the same Cubic Spline technique as for power calculations. The field at the mirror surface is projected onto $\Delta p = 0, \pm 1$ and ± 2 modes to find the complex amplitudes.

Chapter 4

Results

Simulations were made based on observations of Koks [4]. A fixed wavelength of $0.633 \mu m$ was used. Mirrors with curvatures of 5.8 up to $500 \mu m$ were used to simulate different strengths of nonparaxial effects, with a fixed cavity length of $2.2 \mu m$ to ensure $L < R_m/2$. The following chapter will discuss several cases of propagation and compare them to theoretical predictions. Firstly, paraxial propagation to the plane mirror is discussed, which should yield an exact result. After this, 3 different N groups are discussed for nonparaxial propagation to the plane and curved mirror. For each propagation, a figure is inserted to show the field profile at the mirror as well as a table with the difference between the paraxial en average phases for several cavities. Section 4.5 goes beyond reference [4] and tries to find the real eigenmodes of a cavity, by computing the mode coupling amplitudes.

4.1 Paraxial propagation

To check the simulations, a test was conducted propagating the field paraxially. As discussed in the theory section 2.3.1, this problem can be solved analytically and has an exact result. After subtraction of the term $\exp\left(k \frac{r^2}{2R_m}\right)$, we expect to see a uniform phase profile equal to the paraxial phase. Figure 4.1 below shows the phase profile for a cavity with length $L = 2.2 \mu m$ and $R_m = 17.5 \mu m$ of the N=0 mode.

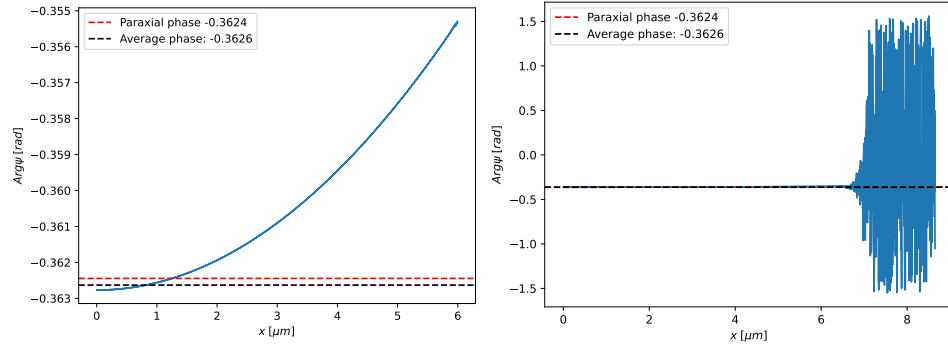


Figure 4.1: Phase profile of the $N=0$ mode propagated paraxially to a plane mirror. The phase is corrected, where the quadratic term $\exp\left(k \frac{r^2}{2R_m}\right)$ (for $R_m = 17.5 \mu m$) has been subtracted. The paraxial and average phases are shown as a reference. $\phi_{RMS} = 0.0001$ [Left]: smaller x -range, [Right]: larger x -range, showing the phase convergence.

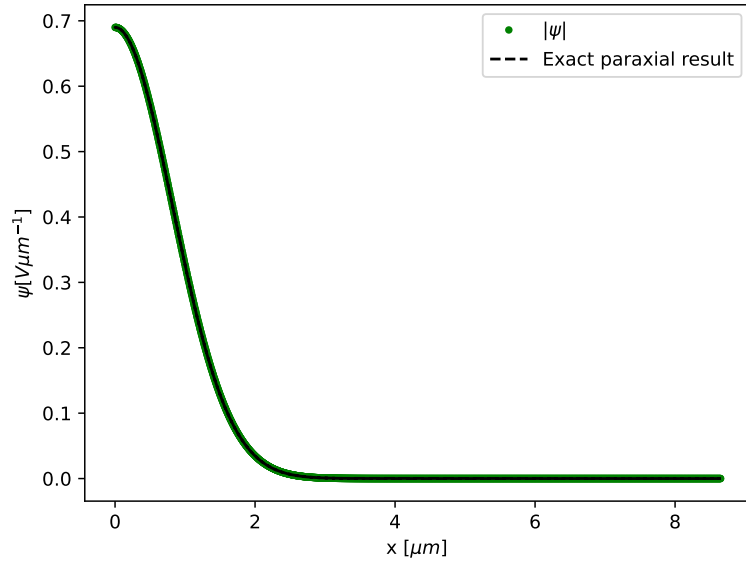


Figure 4.2: Absolute value profile of the $N=0$ mode propagated paraxially to a plane mirror. The exact solution is plotted as a reference.

We can see that the average phase is close to the paraxial phase, with a deviation of 0.0002. For higher x values, (i.e. higher r), the phase increases further. If we increase the x -range, we see that this phase converges to $\pm \frac{\pi}{2}$. At these r -values, the field is practically 0. The phase is calculated by $\phi = \arctan \frac{\text{Im}[\psi]}{\text{Re}[\psi]}$. If the field becomes very small, this quotient can explode to a very large number. Depending on the sign of the real and imaginary part of the field, the program then gives $+$ or $- \frac{\pi}{2}$. We are mainly interested

in the part of the field that is on-axis is or slightly off-axis, as this is where it has an intensity and still has an impact on the average phase calculation, which is intensity-weighted. Figure 4.3 shows the difference between the average and paraxial phase for different nonparaxial strengths and three N-groups.

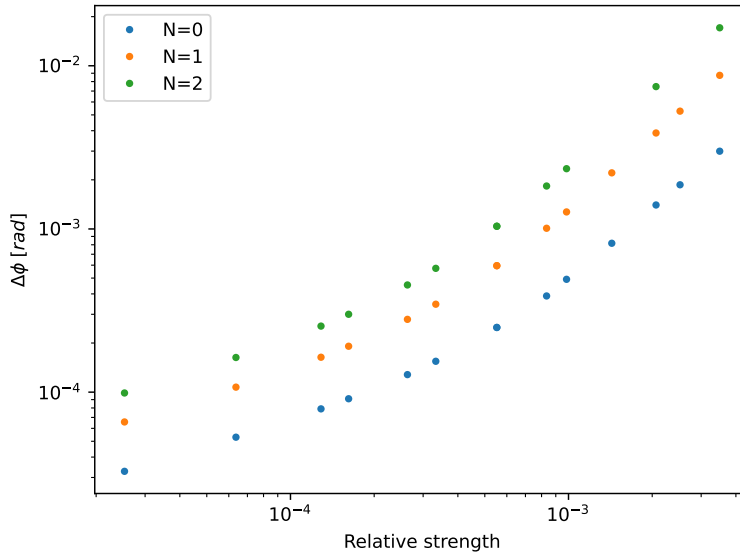


Figure 4.3: Phase difference of average phase and paraxial phase at fixed cavity length ($2.2 \mu\text{m}$) for paraxial propagation to a plane mirror as a function of the relative strength of nonparaxial effects $1/8k(R_m-L)$. Three different N groups are shown.

We can see that for a large radius of curvature, or a small relative strength, this difference becomes almost 0. This is because if $R_m \gg L$, the mirror is almost flat and does not insert a lot of calculation errors. The differences between the different N-groups are also almost negligible for these cases. On the other end of the x-axis, we see larger differences. A relative strength of 0.0035 corresponds to a radius of curvature of $5.8 \mu\text{m}$. The calculation error increases with higher-order modes. Even at the smallest nonparaxial effects the errors are of order 10^{-4} . There is still some sort of instability in the program that causes these errors. What is also notable is the fact that the error increases quadratically on a logarithmic scale, shifted upwards for each N mode. The $N > 0$ modes have a significantly larger error as the strength increases.

4.2 N=0 group

We continued the simulations by propagating the N=0 mode nonparaxially to the curved mirror. Figure 4.4 shows the field profile of the mode at the mirror surface, for $R_m = 17.5 \mu m$. The imaginary part is enhanced 10 times so we can see how it evolves. The phase profile has the average phase subtracted from it, which in the ideal case should yield 0 over the entire mirror surface.

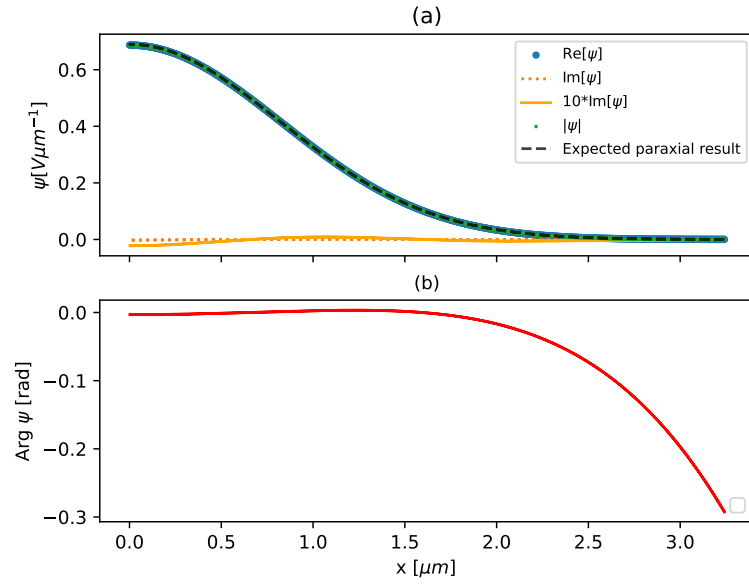


Figure 4.4: Field profile of the N=0 mode at the curved mirror with $R_m = 17.5 \mu m$ and cavity length $L = 2.2 \mu m$. (a) The absolute value of the calculated field profile, where the paraxial solution is plotted as a reference. (b) The corrected phase profile of the field at the mirror.

We can see the same thing happening as in the paraxial case: the phase becomes larger as r increases. Furthermore, by just looking at the graph, the result seems quite accurate and according to expectations. The propagations were repeated for different mirror curvatures, as well as to a plane mirror. The phase difference with respect to the paraxial phase is shown in Table 4.1. Three cases were picked out: $R_m = 5.8, 8.3, 17.3 \mu m$, as done in reference [4].

The wavefront correction deviates more from the theoretical prediction than the propagation correction for stronger effects. The differences are of order 10^{-4} and in some cases even 10^{-3} . This is of the same order of magnitude as the effects we are trying to see.

Table 4.1: Predicted vs simulated phase differences for the N=0 group with $f(p, \ell) = 2$. Each relative strength has two cases, respectively the propagation to the curved mirror (wavefront correction) and to the plane mirror (propagation correction).

$1/8k(R_m-L)$	$\Delta\phi_{theory}$	$\Delta\phi_{calc}$
0.000834	0.0017	0.0017
0.000834	0.0021	0.0019
0.002064	0.0034	0.0041
0.002064	0.0057	0.0052
0.003498	0.0049	0.0070
0.003498	0.0106	0.0097

4.3 N=1 group

The same simulations were done for the N=1 group. When looking at Figure 4.5, it seems that the field at the mirror is in agreement with the paraxial expectation. The corrected phase is approximately 0, after this it starts to decrease again. This is where the absolute value of the field profile is almost 0, so this does not affect further calculations.

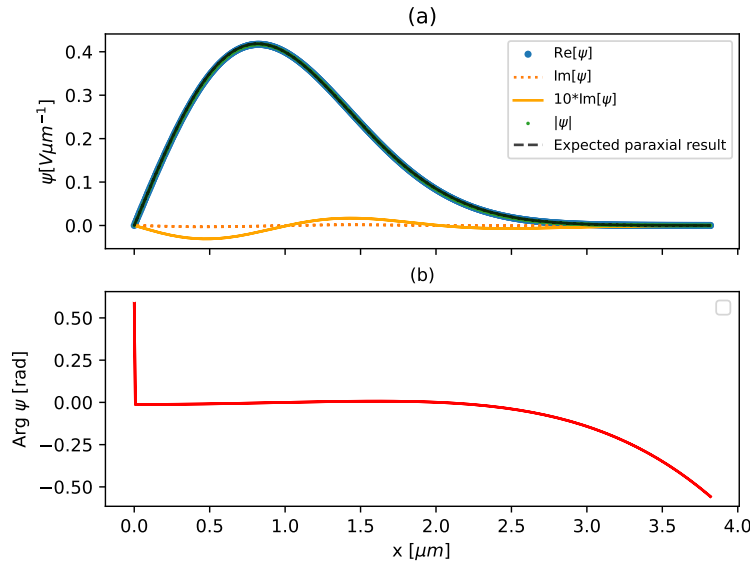


Figure 4.5: Field profile of the N=1 mode at the curved mirror with $R_m = 17.5 \mu m$ and cavity length $L = 2.2 \mu m$. (a) The absolute value of the calculated field profile, where the paraxial solution is plotted as reference. (b) The corrected phase profile of the field at the mirror.

The phase shift with respect to the paraxial phase shows the same behavior as the $N=0$ mode, but much stronger. The wavefront correction is smaller by an order or magnitude with respect to theory. The propagation correction shows errors of the same magnitude as before and is comparable to the predicted phase difference. According to Equation (2.31), the $N=1$ group should have effects that are 3x stronger than those for $N=0$. If we look at the computed numbers for the propagation correction, we do see effects that are roughly three times as large.

Table 4.2: Predicted vs simulated phase differences for the $N=1$ group, with $f(p, \ell) = 6$. Each relative strength has two cases, respectively the propagation to the curved mirror and to the plane mirror.

$1/8k(Rm-L)$	$\Delta\phi_{theory}$	$\Delta\phi_{calc}$
0.000834	0.0050	0.0019
0.000834	0.0056	0.0062
0.002064	0.0157	0.0038
0.002064	0.0124	0.0170
0.003498	0.0290	0.0055
0.003498	0.0289	0.0320

4.4 $N=2$ group

Lastly, the simulations were made for the $N=2$ group, which occurs for 2 cases: $(p=1, \ell=0)$ and $(p=0, \ell=2)$. Here we can see field profiles with a more prominent imaginary part. For both $N=2$ modes, the phase profiles have the same trend: the phase starts to slightly decrease and then converges to $\pm \frac{\pi}{2}$ for high r -values. The phase of the $p=1$ mode shows a small nod at around $x=1$. This happens as the imaginary part changes sign for a short period, possibly giving an instability in the arctan function.

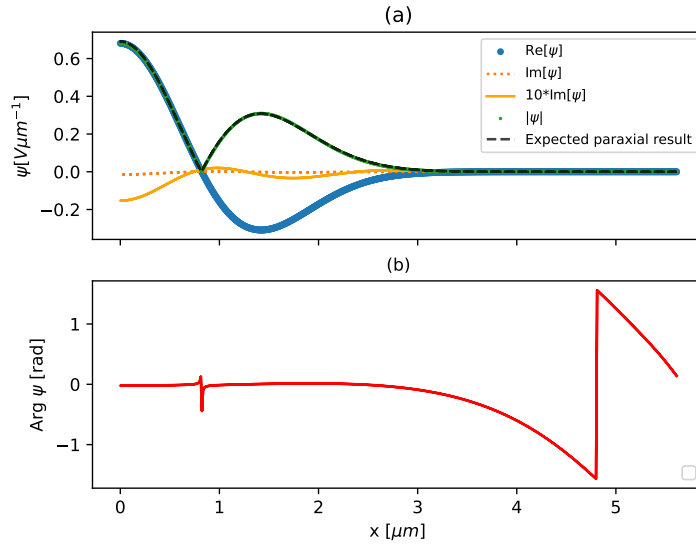
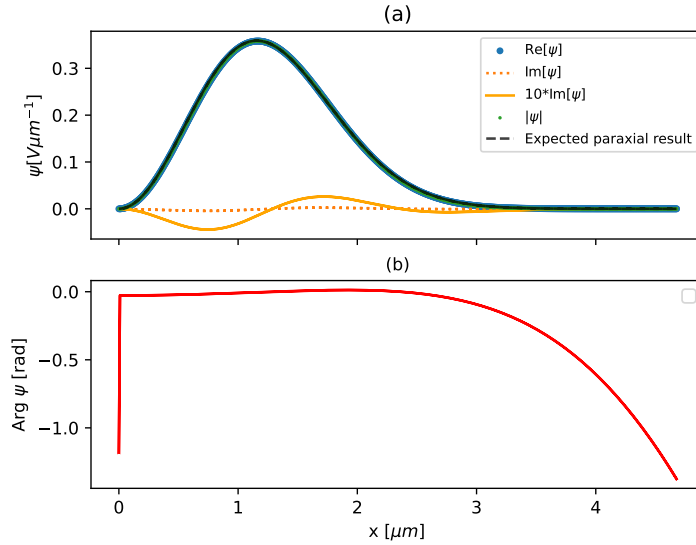
(i) $p=1, \ell=0$ mode(ii) $p=0, \ell=2$ mode

Figure 4.6: Field profile of the $N=2$ modes at the curved mirror with $R_m = 17.5 \mu m$ and cavity length $L = 2.2 \mu m$. [Above]: ($p=1, \ell=0$). [Below]: ($p=0, \ell=2$) (a) The absolute value of the calculated field profile, where the paraxial solution is plotted as reference. (b) The corrected phase profile of the field at the mirror.

Again, the wavefront correction deviates more from theory than the propagation correction. For the computed values, the scaling with $f(p, \ell)$

is as expected, but still differs from theoretical values with $\propto 10^{-3}$. For the $(p=1, \ell=0)$ mode, however, the wavefront correction is of the same order of magnitude, but 2-3 times smaller. The same correction for the $(p=0, \ell=2)$ mode seems to go to 0, this could indicate an instability for $\ell > 0$ modes, as the same behavior is seen in the $N=1$ $(p=0, \ell=1)$ mode. This could occur because the vector correction has not yet been implemented, which also includes effects for the orbital angular momentum ℓ .

Table 4.3: Predicted vs simulated phase differences for the $N=2$ group $(p=1, \ell=0)$ mode), with $f(p, \ell) = 14$. Each relative strength has two cases, respectively the propagation to the curved mirror and to the plane mirror.

$1/8k(Rm-L)$	$\Delta\phi_{theory}$	$\Delta\phi_{calc}$
0.000834	0.0100	0.0053
0.000834	0.0112	0.0143
0.002064	0.0248	0.0109
0.002064	0.0313	0.0444
0.003498	0.0420	0.0157
0.003498	0.0579	0.0767

Table 4.4: Predicted vs simulated phase differences for the $N=2$ group $(p=0, \ell=2)$ mode), with $f(p, \ell) = 12$. Each relative strength has two cases, respectively the propagation to the curved mirror and to the plane mirror.

$1/8k(Rm-L)$	$\Delta\phi_{theory}$	$\Delta\phi_{calc}$
0.000834	0.0117	0.0008
0.000834	0.0132	0.0123
0.002064	0.0289	0.0014
0.002064	0.0366	0.0376
0.003498	0.0490	0.0018
0.003498	0.0676	0.0651

4.5 Modal decomposition

Mode coupling up to $|\Delta p| = 2$ was computed for the $N=0,1$ and 2 modes for the same curvatures as before. The results are shown in Tables 4.5, 4.6 and 4.7 respectively.

For $N=0$, the dominant mode has an amplitude of $> 99\%$. The higher order modes mix in with much smaller amplitudes but differ quite a lot from the predictions. The $\Delta p = 1$ mode has the same order of magnitude but still has a significant deviation from the expectations. The $\Delta p = 2$ mode mixes in with a larger amplitude than $\Delta p = 1$, which is not in line with theory. Unfortunately, no better simulations were made for the mode mixing amplitudes. This still remains a challenge, but is a nice route to find the real eigenmodes of the cavity.

Table 4.5: Calculated vs expected amplitudes of mode mixing for the $N=0$ group

$1/8k(Rm-L)$	$\Delta p = 0$	$\Delta p = 1$ /Prediction	$\Delta p = 2$ /Prediction
0.000834	0.998859	0.001386	0.003336
0.002064	0.996180	0.006273	0.008258
0.003498	0.992863	0.013443	0.013992

The mode coupling amplitudes of $N=1$ show the same behaviour as $N=0$. $\Delta p = 1$ coupling amplitudes are of the same order of magnitude as expected, with for the $N=1$ group even more in agreement with predictions. $\Delta p = 2$ again shows a coupling an order of magnitude larger than expected.

Table 4.6: Calculated vs expected amplitudes of mode mixing for the $N=1$ group

$1/8k(Rm-L)$	$\Delta p = 0$	$\Delta p = 1$ /Prediction	$\Delta p = 2$ /Prediction
0.000834	0.997673	0.003943	0.004718
0.002064	0.992204	0.011972	0.011678
0.003498	0.985281	0.021994	0.019788

In Table 4.7, the two different modes are paired together, with the upper being $p=1$ and the lower $p=0$. We can again see significant deviations from theoretical predictions. For example, the $\Delta p = -1$ coupling should be the same as $p = 1$ for the $N=0$ mode, according to Equation (2.37), but when comparing the two cases, the program gives completely different amplitudes.

Table 4.7: Calculated vs expected amplitudes of mode mixing for the N=2 group. Each relative strength has its own pair of N=2 modes, respectively the $(p=1, \ell=0)$ and $(p=0, \ell=2)$ modes. The modes are ordered from low to high nonparaxial effects.

$\Delta p = 0$	$\Delta p = -1$ /Prediction	$\Delta p = 1$ /Prediction	$\Delta p = 2$ /Prediction
0.996355	0.009423	0.003336	0.009776
0.996447	-	-	0.013344
0.987593	0.026738	0.008256	0.005778
0.988011	-	-	0.0185176
0.976409	0.043405	0.013992	0.022690
0.977279	-	-	0.005004
			0.014303
			0.055920
			0.113169
			0.020989
			0.017137

Chapter 5

Discussion

The simulation outcomes were presented in the previous chapter. In short, we can say that the program shows a promising potential to solve the fine-structure problem, but still needs to be fine-tuned in some places. Firstly, the paraxial propagation to the plane mirror fails to give an exact result. The average phase is off by a magnitude of 10^{-4} . As we are trying to find nonparaxial effects of this order of magnitude, it would be ideal to get this error down by two orders of magnitude.

It's difficult to find the exact weak spot of the simulations. Lots of intermediate steps were made before finding the field profile at the mirror. Firstly, the initial field profiles are defined at $z=0$. This is done by a Numpy method that has defined Laguerre polynomials. These are produced by a differential equation that needs to be solved and while this can be done numerically, it already introduces some errors. After this, the field profile is propagated using a discrete Fourier transform. Scipy's `fft` algorithm makes this an efficient calculation, but the accuracy of discrete Fourier transforms is dependent on the type of grid used. These effects were described in section 3.3.2. The `fft` algorithm also calculates the frequencies present (k_{\perp}) and from this the propagation vector $\exp(ik_z z)$ is computed. Then, an inverse FT is performed on the product of this vector with the transformed field profile. All these calculation steps individually introduce some, presumably $\propto \frac{1}{N}$ or $\frac{1}{N^2}$ with N the grid size.

After the propagation, more calculations are made on the field profile. We want to know how the average phase is related to the expected paraxial phase. To calculate this average phase, a numerical integral needs to be computed that calculates the intensity-weighted average phase. We saw in section 3.2.2 that this introduces errors of $\propto \frac{1}{N^2}$. Another problem we see is that for the outer regions of the mirror (large r), the magnitude of the phase

starts to grow and converges to $\pm \frac{\pi}{2}$. A possible explanation for this is the fact that the phase needs to be calculated by a quotient of the imaginary and real part of the field profile. Overall, the imaginary part is quite small, but as r grows, the real part becomes really small as well. This could cause some instability in the quotient, as division by a really small number can be interpreted as division by 0 by a computer. This causes the arctan function to grow slowly until it reaches $\frac{\pi}{2}$.

The simulations were done with mirrors of different curvatures, to try and find the fine spectrum of the FP cavity. The paraxial propagation shows an increase in error for a smaller radius of curvature. This could be caused by the fact that as $R_m/2 \rightarrow L$, the simulations become more unstable. For higher N-modes, this error even increases to an order of 10^{-2} , as shown in Figure 4.3. The error shows a quadratic increase on a logarithmic scale. The nature of how this error scales is still unknown.

For nonparaxial propagation, we saw that the phase difference for the propagation correction was in agreement with theoretical predictions, but still deviates by factors of the same order of magnitude as the effects themselves. This could be nested in the error of 10^{-4} for the paraxial propagation. We do see a scaling of the computed propagation phase differences by the expected polynomial $f(p, \ell)$. The computed wavefront corrections are much smaller than we would expect for all N modes. We also see that for $\ell > 0$ modes, the wavefront corrections go to 0. This could be caused by a missing $\ell \cdot s$ factor from the vector correction, which has not been implemented yet. The program gives promising results for propagation corrections. If the calculation errors can be decreased by a couple of orders of magnitude, we would be able to compare the numbers in more detail. A full description of the problem is still incomplete, so we cannot yet draw conclusions about the full fine spectrum of the cavities.

To try and find the 'real' eigenmodes or eigenfunctions of the problem, the modal decomposition of the field profile was computed. Equation (2.37) describes the predicted mode coupling amplitudes which should scale with $1/8k(R_m - L)$. Tables 4.5, 4.6 and 4.7 show these mode couplings for $1/8k(R_m - L) = 0.000834, 0.002064$ and 0.003498 . We would expect the dominant mode ($\Delta p = 0$) to have a coupling amplitude ≈ 1 . This is true for all cases, which indicates that the chosen modes are a good basis for the problem. The other modes are expected to mix in with smaller amplitudes. Overall we observe that the $\Delta p = 1$ mode mixing gives values of the same order of magnitude as theory predicts, but the deviations are still large. $\Delta p = -1$ and $\Delta p = 2$ modes are more off, with the $\Delta p = 2$ mode even being an order of magnitude larger than expected. If we look at the sum of the intensities of the modal amplitudes, we would expect them to

be equal to the power of the mode, as Equation (2.39) suggests. If we take the $N=0$ mode, for example, the intensities add up to 0.997732, 0.992908, 0.987345 for increasing relative strength, instead of the total power of the field which is 0.999985. This may suggest that some other underlying discretization problem is present in the program.

5.1 Simulation challenges

A lot of challenges were faced when creating the simulation program. We already mentioned the switch in propagation method, as we found out that the discretization of the Helmholtz equation (2.10) described in Appendix A was not providing the wanted results. We quickly decided to switch to Fourier propagation. Another important evolution of the program was the object-oriented approach that helped with the readability of the code and the traceback of errors.

A big simulation challenge we faced was numerical integration, which is especially important for modal decomposition. Integration tricks from Numerical recipes [15] were implemented and in the end, a choice was made for Cubic Spline interpolation as an integration method. This gave an error on the power of the field $\propto 10^{-5}$, see Table 3.1. What was also tested, was the projection of the paraxial field profiles. A projection of the 00 modes on itself yields the power calculation. When we project a mode onto another mode with a different radial number p , we expect an output of 0. The program gave an output of $\approx 10^{-6}$. This is quite small, but should ideally still be a couple of orders of magnitude smaller. This could be an issue with the initial definition of the Laguerre-Gauss modes in the Mode class.

Overall, the program can use some improvements that could lead to reproducing the fine spectrum of an optical microcavity. The program has some fundamental issues as it cannot solve the paraxial case exactly. We have discussed some parameters that had been tested and improved, but this has not led to the exact solution yet. The inability of the program to solve the exact case introduces errors of the same order of magnitude as the effects we try to measure in the fine spectrum. There are also still discretization errors present despite the large grid size, which lead to unexpected results in the modal decomposition. After reproducing this fine spectrum, we could go on to solve harder problems that are challenging to reproduce in a lab.

5.2 Outlook

There are some problems to be solved that are beyond the scope of the program. For example, in a lab, there are no perfect mirrors. Mirrors can create Bragg effects that can shift the fine structure. Also, mirrors could be astigmatic, meaning their radius of curvature in the x- and y-directions are not the same. This breaks the rotational symmetry and would need a full 2D analysis to solve. These are possible extensions to the program that could reproduce a lab environment. Another extension to be made is the composite cavity. This cavity has an intermediate interface that can also shift the resonance frequencies. A full analysis of this problem is still missing and could be supported by simulations. The program has yet to achieve reliable accuracy, but if we are able to reproduce the fine structure of higher-order N-modes, it would be interesting to look at unknown problems. We could also go beyond the scope of Koks [4] and try to find a full description of the eigenmodes of the cavity. A first step was made by calculating the modal decomposition of the cavity, but it is beyond complete.

Conclusions

This thesis provided software for computing the fine spectrum of a Fabry-Pérot microcavity. Results for nonparaxial propagation show potential in the program to identify the propagation corrections, but a complete description is missing. We also looked at the bigger picture and introduced the modal decomposition, which is a way to find the real eigenmodes of the cavity. The modal decomposition theory provides the coupling amplitudes to expect from nonparaxial effects. We found that the dominant mode mixes in with the largest amplitude, which is close to 1 and that other modes mix in with much smaller amplitudes. The $\Delta p = 1$ modes showed a coupling of the expected order of magnitude, but still off from theoretical predictions. $\Delta p = 2$ couplings turned out to be larger than expected.

We learned that propagation using the angular spectrum method provides more stable results and that an object-oriented approach is much more efficient for the computations. The program still needs some improvements in accuracy and stability, but already shows some results that can be compared to theory. Currently, only scalar effects are presented. The vector correction still needs to be implemented. If fine-tuned in the right places, possible expansions to astigmatic mirrors, Bragg effects, and even composite cavities can be made to support experimental observations and assist theoretical expectations.

Alternative route: Finite element analysis

Besides the plane wave decomposition, another method to solve the propagation equation was implemented. Equation (2.20) was discretized using techniques from reference [15]. The equation can be rewritten in the form

$$\frac{\partial}{\partial z} \psi = \frac{i}{2k} \left(\frac{\partial^2}{\partial r^2} + \frac{1}{r} \frac{\partial}{\partial r} \right) \psi \quad (\text{A.1})$$

This resembles a diffusion equation, where z acts as a time-coordinate and the spatial coordinate r combines two-dimensional Cartesian space x and y into one coordinate. Two models were made: a finite difference model and a finite volume model. For both of the methods, a grid in the r - and z -directions is created on which the function ψ exists. The spacing on the grid is given by Δr and Δz . Each point on the grid is denoted by $\vec{\psi}_i^n$, where i denotes the position on the r -grid and n denotes the position on the z -grid. The differential operator can be rewritten as an $(N-1) \times (N-1)$ matrix D with N the grid size, where the off-diagonal elements denote the dependency of $\vec{\psi}_i$ on $\vec{\psi}_{i-1}$ and $\vec{\psi}_{i+1}$. We want to find an expression for a step in the z -direction $\vec{\psi}_i^{n+1}$. Equation (A.1) can be rewritten in the discretized form

$$\vec{\psi}_i^{n+1} = D \cdot \vec{\psi}_i^n \quad (\text{A.2})$$

Important to note is that the matrix D must be a unitary operator, or a Hermitian matrix, as there is no power loss in propagation. This can be solved using the Crank-Nicolson method [15]. It states that for a differential equation of the form

$$-i \frac{\partial}{\partial z} \psi = H \cdot \psi \quad (\text{A.3})$$

with H a unitary matrix, the solutions are of the form

$$\psi(r, z) \propto e^{iHz} \cdot \psi(r, 0) \quad (\text{A.4})$$

The matrix e^{iHz} can be rewritten as

$$e^{iHz} = \frac{I + \frac{1}{2}iH\Delta z}{I - \frac{1}{2}iH\Delta z} \quad (\text{A.5})$$

Now we can rewrite the discretized differential equation as

$$\begin{aligned} \psi_i^{n+1} \cdot \left[I - \frac{1}{2}iH\Delta z \right] &= \psi_i^n \cdot \left[I + \frac{1}{2}iH\Delta z \right] \\ \psi_i^{n+1} &= \psi_i^n \cdot \left[I + \frac{1}{2}iH\Delta z \right] \left[I - \frac{1}{2}iH\Delta z \right]^{-1} \end{aligned} \quad (\text{A.6})$$

For the finite-difference method, the matrix H was derived to be

$$H_{FD} = \frac{1}{(\Delta r)^2} \begin{pmatrix} -2 & 2 & 0 & \dots & 0 \\ 1 - \frac{1}{n} & \dots & 1 + \frac{1}{n} & & \\ 0 & 1 - \frac{1}{n} & & 1 + \frac{1}{n} & \\ \dots & 0 & \dots & & \\ & \dots & & 1 - \frac{1}{n} & 1 + \frac{1}{n} \\ 0 & 0 & 0 & \dots & -2 \end{pmatrix} \quad (\text{A.7})$$

Here, the main diagonal element is $\frac{-2}{(\Delta r)^2}$, the lower-diagonal $\frac{1}{(\Delta r)^2} (1 - \frac{1}{n})$ and the upper-diagonal $\frac{1}{(\Delta r)^2} (1 + \frac{1}{n})$. For the finite-volume method, the matrix H was

$$H_{FV} = \frac{1}{(\Delta r)^2} \begin{pmatrix} 2(r_i + \frac{1}{\Delta r}) & 1 & 0 & \dots & 0 \\ -r_i & & r_i & & \\ 0 & -r_i & 0 & r_i & \\ \dots & 0 & \dots & & \\ & \dots & & -r_i & r_i \\ 0 & 0 & 0 & \dots & 2(r_i + \frac{1}{\Delta r}) \end{pmatrix} \quad (\text{A.8})$$

with main-diagonal $\frac{(r_i + \frac{1}{\Delta r})}{(\Delta r)^2}$, lower-diagonal $\frac{-r_i}{(\Delta r)^2}$ and upper-diagonal $\frac{r_i}{(\Delta r)^2}$.

In both matrices, a term $\frac{1}{(\Delta r)^2}$ appears. This term is very small and causes instabilities. For both matrices, the off-diagonal elements are small in comparison to the on-diagonal elements. With each propagation step, the matrix operation is applied again, making the off-diagonal elements smaller with each step. After a few steps, these are almost negligible and the matrix $H \rightarrow I$ as $n \rightarrow N$. We saw that the propagation gave the same result at $z=L$ as at $z=0$ and decided to continue with the Angular Spectrum method for field propagation.

Appendix **B**

Supplementary documentation on the simulation program

This appendix includes documentation of the code, describing all objects and routines in more detail. It is also available as `README.md` in the Github repository. All length units are in microns.

B.1 Objects file

B.1.1 Geometry

This object determines the geometry of the problem. It consists of the wavelength, of the cavity, radius of curvature, a factor `pwig` that determines the shape of the mirror and grid size. From this, a grid for the x coordinates is made.

Extra feature possibilities: asymmetric mirrors, with a different radius of curvature in the x and y direction.

Routines

`get_2D_grid`: Returns a 2D cartesian grid, which is symmetric in the x and y direction.

`get_mirror_coords`: returns the mirror's z coordinates

`get_mirror_planes`: returns 4 evenly spaced z-planes around the mirror surface, used in the propagation routines (explained later)

B.1.2 Field

Base class, containing a geometry and field profile. The absolute value, intensity, real and imaginary part and phase are defined.

Field 1D

Field derived class, containing a 1D field profile, which is a 2D profile corss-sectioned at $y=0$. It has an extra feature: the on-axis-phase, which is the phase of the field at $r=0, z=L$.

Routines

power: calculates the 1D power, weighted over the intensity. Fields are normalized, so this is a unitarty operation check

phase_moments: calculates the intensity-weighted average and RMS phase

phase_shift: shifts the profile over the average phase.

phase_plate: used for plane propagation, adds a phase plate factor that corrects the phase of the propagation, by adding a phase lag of $k \cdot z_m$.

Field2D

Field derived class, containing a 2D field profile.

Routines:

power: calculates the power. Fields are normalized, so this is a unitarty operation check

cross_section: returns a 1D field, which is a cross-section at $y=0$ of the 2D field profile.

B.1.3 Mode

A paraxial mode in the LG (orthonormal) basis. Defined by p and l modal numbers, geometry and paraxial/non-paraxial propagation. The modal number N , Rayleigh range z_0 and beam width w_0 are calculated from these parameters.

Routines:

field_profile: calculates the field profile, as a normalized LG mode at a z coordinate. The default is $z=0$, i.e the field at the flat mirror. If a different z -coordinate is given, for example $z=L$, it returns the paraxial expectation of the field at that z plane.

get_gouy: returns the gouy phase at a certain z coordinate.

FFT2D: propagates the initial field from $z=0$ to a different z plane, using the angular spectrum method.

propagate_mirr: propagates the initial field, using the angular spectrum method, to the mirror surface, by interpolation.

`propagate_plane`: propagates the initial field, using the angular spectrum method, to the $z=L$ plane and used a phase plate to correct for the mirror.

B.1.4 Other routines outside classes

projection

Projects the field profile on the mirror surface onto a different p mode.

modal decomposition

Calculates the projection of the electric field on the mirror to the $LG\{lp\}$ basis. (up to $\Delta p = \pm 2$) Returns the values of p , α and the projected modes.

expected_coupling

Returns an array of the expected mode coupling for a certain (p,l) mode and relative strength $1/8k(R_m-L)$

B.2 Plot routines file

Creates plots depending on mirror/plane propagation.

B.2.1 `plot_intensity`

Plots the intensity of a 2D field object with colorbar.

B.2.2 `plot_mirr`

Creates plots of the field profile for propagation to the curved mirror and the corrected phase as in Figures 4.4, 4.5 and 4.6.

B.2.3 `plot_plane`

Creates a plot of the corrected phase for propagation to a plane mirror, as in Figure 4.2.

B.2.4 `plot_decomposition`

Plots the modal decomposition of a field profile as well as the field profile itself for comparison.

B.3 Main file

This file contains the main program, from which the simulations are run. It defines the geometry parameters wavelength, L, Rm, grid_size and pwig. You can also select the desired (p,l) mode and a Mode object is created from this. A paraxial variable is created to turn the paraxial propagation ON/OFF. The program computes the curved and plane mirror propagation and calculates the modal decomposition.

Bibliography

- [1] A. E. Siegman. *Lasers*. University Science Books, 1 1986.
- [2] Kerry J. Vahala. Optical microcavities. *Nature*, 424(6950):839–846, 8 2003.
- [3] Edward Hissink, C. Koks, and M. P. Van Exter. Nonparaxial corrections for short cavities and fibers. *Physical review*, 106(5), 11 2022.
- [4] C. H. W. Koks, F. B. Baalbergen, and M. P. Van Exter. Observation of microcavity fine structure. *Physical review*, 105(6), 3 2022.
- [5] Melvin Lax, William H. Louisell, and William B. McKnight. From Maxwell to paraxial wave optics. *Physical Review A*, 11(4):1365–1370, 4 1975.
- [6] C.W. Erickson. High order modes in a spherical fabry-perot resonator. *IEEE Transactions on Microwave Theory and Techniques*, 23(2):218–223, 1975.
- [7] A. L. Cullen. On the accuracy of the beam-wave theory of the open resonator. *IEEE Transactions on Microwave Theory Techniques*, 24:534, August 1976.
- [8] L.W. Davis. Vector electromagnetic modes of an optical resonator. *Phys. Rev. A*, 30(6):3092–3096, 1984.
- [9] P.K. Yu and K-M. Luk. Field patterns and resonant frequencies of high-order modes in an open resonator (short papers). *IEEE Transactions on microwave theory and techniques*, 32(6):641–645, 1984.
- [10] M. P. Van Exter, M. Wubs, E. Hissink, and C. H. W. Koks. Fine structure in Fabry-Perot microcavity spectra. *Physical review*, 106(1), 7 2022.

- [11] Kyoji Matsushima, Hagen Schimmel, and Frank Wyrowski. Fast calculation method for optical diffraction on tilted planes by use of the angular spectrum of plane waves. *J. Opt. Soc. Am. A*, 20(9):1755–1762, Sep 2003.
- [12] Jin Au Kong. *Electromagnetic Wave Theory*. E M W Pub, 6 2000.
- [13] Marco W. Beijersbergen, L. Allen, H.E.L.O. Van Der Veen, and J. P. Woerdman. Astigmatic laser mode converters and transfer of orbital angular momentum. *Optics Communications*, 96(1-3):123–132, 2 1993.
- [14] Fabian Shen and Anbo Wang. Fast-Fourier-transform based numerical integration method for the Rayleigh-Sommerfeld diffraction formula. *Applied optics*, 45(6):1102, 2 2006.
- [15] William H. Press, Saul A. Teukolsky, William T. Vetterling, and Brian P. Flannery. *Numerical Recipes 3rd Edition*. Cambridge University Press, 9 2007.
- [16] Charles R. Harris, K. Jarrod Millman, Stéfan J van der Walt, Ralf Gommers, Pauli Virtanen, David Cournapeau, Eric Wieser, Julian Taylor, Sebastian Berg, Nathaniel J. Smith, Robert Kern, Matti Picus, Stephan Hoyer, Marten H. van Kerkwijk, Matthew Brett, Allan Haldane, Jaime Fernández del Río, Mark Wiebe, Pearu Peterson, Pierre Gœrard-Marchant, Kevin Sheppard, Tyler Reddy, Warren Weckesser, Hameer Abbasi, Christoph Gohlke, and Travis E. Oliphant. Array programming with NumPy. *Nature*, 585:357–362, 2020.
- [17] M P van Exter, E S Hissink, and C Koks. From effective-index model to phase-plate model. *Journal of Optics*, 24(8):084001, jun 2022.
- [18] Pauli Virtanen, Ralf Gommers, Travis E. Oliphant, Matt Haberland, Tyler Reddy, David Cournapeau, Evgeni Burovski, Pearu Peterson, Warren Weckesser, Jonathan Bright, Stéfan J. van der Walt, Matthew Brett, Joshua Wilson, K. Jarrod Millman, Nikolay Mayorov, Andrew R. J. Nelson, Eric Jones, Robert Kern, Eric Larson, C J Carey, İlhan Polat, Yu Feng, Eric W. Moore, Jake VanderPlas, Denis Laxalde, Josef Perktold, Robert Cimrman, Ian Henriksen, E. A. Quintero, Charles R. Harris, Anne M. Archibald, Antônio H. Ribeiro, Fabian Pedregosa, Paul van Mulbregt, and SciPy 1.0 Contributors. SciPy 1.0: Fundamental Algorithms for Scientific Computing in Python. *Nature Methods*, 17:261–272, 2020.
- [19] Richard Baraniuk. *Signals and Systems*. 2008.